The Astronomical Journal, 159:40 (15pp), 2020 February https://doi.org/10.3847/1538-3881/ab5afa

Atmospheric Characterization and Further Orbital Modeling of κ Andromeda b

Taichi Uyama[1,2,3,4], Thayne Currie[5,6,7], Yasunori Hori[4,8], Robert J. De Rosa[9], Kyle Mede[3], Timothy D. Brandt[10], Jungmi Kwon[3], Olivier Guyon[6,8,11], Julien Lozi[6], Nemanja Jovanovic[12], Frantz Martinache[13], Tomoyuki Kudo[6], Motohide Tamura[3,4,8], N. Jeremy Kasdin[14], Tyler Groff[15], Jeffrey Chilcote[16], Masahiko Hayashi[4], Michael W. McElwain[15], Ruben Asensio-Torres[17], Markus Janson[17], Gillian R. Knapp[18], and Eugene Serabyn[19]

[1] Infrared Processing and Analysis Center, California Institute of Technology, Pasadena, CA 91125, USA
[2] NASA Exoplanet Science Institute, Pasadena, CA 91125, USA
[3] Department of Astronomy, The University of Tokyo, 7-3-1, Hongo, Bunkyo-ku, Tokyo 113-0033, Japan
[4] National Astronomical Observatory of Japan, 2-21-1 Osawa, Mitaka, Tokyo 181-8588, Japan
[5] NASA-Ames Research Center, Moffett Field, CA, USA
[6] Subaru Telescope, National Astronomical Observatory of Japan, 650 North A'ohoku Place, Hilo, HI 96720, USA
[7] Eureka Scientific, 2452 Delmer Street Suite 100, Oakland, CA, USA
[8] Astrobiology Center of NINS, 2-21-1 Osawa, Mitaka, Tokyo 181-8588, Japan
[9] Kavli Institute for Particle Astrophysics and Cosmology, Stanford University, Stanford, CA 94305, USA
[10] Department of Physics, University of California, Santa Barbara, Santa Barbara, CA, USA
[11] Steward Observatory, University of Arizona, Tucson, AZ 85721, USA
[12] Department of Astronomy, California Institute of Technology, 1200 East California Boulevard, Pasadena, CA 91125, USA
[13] Université Côte d'Azur, Observatoire de la Côte d'Azur, CNRS, Laboratoire Lagrange, France
[14] Department of Mechanical Engineering, Princeton University, Princeton, NJ, USA
[15] NASA-Goddard Space Flight Center, Greenbelt, MD, USA
[16] Department of Physics, University of Notre Dame, South Bend, IN, USA
[17] Department of Astronomy, Stockholm University, AlbaNova University Center, SE-106 91 Stockholm, Sweden
[18] Department of Astrophysical Science, Princeton University, Peyton Hall, Ivy Lane, Princeton, NJ 08544, USA
[19] Jet Propulsion Laboratory, California Institute of Technology, Pasadena, CA 91109, USA
Received 2019 August 12; revised 2019 November 16; accepted 2019 November 21; published 2020 January 7

Abstract

We present κ Andromeda b's photometry and astrometry taken with Subaru/SCExAO+HiCIAO and Keck/NIRC2, combined with recently published SCExAO/CHARIS low-resolution spectroscopy and published thermal infrared photometry to further constrain the companion's atmospheric properties and orbit. The $Y/Y-K$ colors of κ And b are redder than field dwarfs, consistent with its youth and lower gravity. Empirical comparisons of its Y-band photometry and CHARIS spectrum to a large spectral library of isolated field dwarfs reaffirm the conclusion from Currie et al. that it likely has a low gravity but admit a wider range of most plausible spectral types (L0–L2). Our gravitational classification also suggests that the best-fit objects for κ And b may have lower gravity than those previously reported. Atmospheric models lacking dust/clouds fail to reproduce its entire 1–4.7 μm spectral energy distribution (SED), and cloudy atmosphere models with temperatures of $\sim$1700–2000 K better match κ And b data. Most well-fitting model comparisons favor 1700–1900 K, a surface gravity of $\log(g) \sim 4$–4.5, and a radius of 1.3–1.6 $R_{\rm Jup}$; the best-fit model (DRIFT-PHOENIX) yields the coolest and lowest-gravity values: $T_{\rm eff} = 1700$ K and $\log g = 4.0$. An update to κ And b's orbit with ExoSOFT using new astrometry spanning 7 yr reaffirms its high eccentricity (0.77 ± 0.08). We consider a scenario where unseen companions are responsible for scattering κ And b to a wide separation and high eccentricity. If three planets, including κ And b, were born with coplanar orbits, and one of them was ejected by gravitational scattering, a potential inner companion with mass $\gtrsim$10 $M_{\rm Jup}$ could be located at $\lesssim$25 au.

Unified Astronomy Thesaurus concepts: Exoplanet astronomy (486); Exoplanet evolution (491); Exoplanet atmospheres (487); Exoplanet formation (492)

1. Introduction

With the development of adaptive optics (AO), direct imaging has uniquely been probing exoplanet populations of young and wide-orbit gas giants (e.g., Lagrange et al. 2010; Marois et al. 2010; Kuzuhara et al. 2013; Currie et al. 2015; Macintosh et al. 2015; Keppler et al. 2018). Young gas giants are amenable to direct detection at infrared wavelengths, as they are still radiating away their heat of formation, which means that these planets still have vestiges of planet formation and are bright enough to be resolved with high-contrast imaging instruments around nearby bright stars.

Photometric and low-resolution spectroscopic measurements of directly imaged planets and young substellar objects can be used to estimate bulk atmospheric properties. Broadband (spectro)photometry over a wide wavelength range can reveal young planet/brown dwarf atmospheres that are cloudier and/or dustier than isolated field substellar objects of the same temperatures (Currie et al. 2011, 2013; Liu et al. 2013; De Rosa et al. 2016; Rajan et al. 2017). Spectral shapes in the major near-IR passbands can diagnose evidence for low surface gravity in young objects (Kirkpatrick et al. 2006; Allers & Liu 2013; Currie et al. 2014b). Well-calibrated, high signal-to-noise ratio (S/N) spectra for isolated young and field brown dwarfs can help constrain the spectral type and gravity classification of directly imaged exoplanets (e.g., Bonnefoy et al. 2016; Chilcote et al. 2017; Currie et al. 2018). Atmospheric modeling provides a constraint on the temperature, cloud structure, luminosity, and (possibly) gravity of imaged exoplanets (e.g., Currie et al. 2011; Barman et al. 2015; Chilcote et al. 2017; Rajan et al. 2017).

Previous studies have shown that in situ core accretion (Pollack et al. 1996) or gravitational instability (Boss 2011)

Table 1
Adopted Stellar Parameters for κ And

Parameters	κ And	Reference
R.A.	23:40:24.506	(1)
Decl.	+44:20:02.18	(1)
Sp. type	B9	(2), (3)
Mass [$M_{\odot}$]	2.6–2.8	(2), (3), (4)
Age [Myr]	47^{+27}_{-40}	(2)
Distance [pc]	50.0 ± 0.1	(1)

References. (1) Gaia Collaboration et al. (2018). (2) Jones et al. (2016). (3) Currie et al. (2018). (4) Bonnefoy et al. (2014b).

scenarios struggle to reproduce mass–semimajor axis distributions of the observed planets beyond ∼10 au (e.g., Boley 2009; Currie et al. 2011). Therefore, gravitational scattering between planets is proposed to assist formation of wide-orbit planets in the core accretion process (e.g., Marzari & Weidenschilling 2002; Ford & Rasio 2008; Nagasawa et al. 2008). Detecting counterparts that were involved in planet–planet scattering, however, is difficult. The number of confirmed directly imaged planets (∼10–20) impedes our ability to constrain their formation and evolution scenarios; current frequencies of giant planets beyond ∼10 au derived from direct imaging surveys are ∼10% or less (e.g., Brandt et al. 2014; Bowler 2016; Uyama et al. 2017; Nielsen et al. 2019). Thus, continuous efforts to directly image and characterize wide-orbit planetary systems around young stars are essential to understand the formation mechanisms of wide-orbit planets.

In this study, we target a bright, young, and nearby B9V star, κ And (see Table 1 for the stellar parameters). The Strategic Explorations of Exoplanets and Disks with Subaru (Tamura 2009) reported that κ And harbors a substellar-mass companion (κ And b; Carson et al. 2013). While early studies admit a wide range of potential ages for the system (Carson et al. 2013; Hinkley et al. 2013; Bonnefoy et al. 2014b), follow-up studies showed that the system is young, with a likely age of ∼40 Myr (Jones et al. 2016) and kinematics that might be consistent with membership in the ∼20–50 Myr old Columba association (Currie et al. 2018). Early SED modeling of κ And b's photometry from J through M' (1.25–5 μm) suggested the companion had a temperature of 1700–2000 K but could not constrain its surface gravity (Bonnefoy et al. 2014b). Near-infrared Subaru/SCExAO+CHARIS spectroscopy of κ And b from Currie et al. (2018) showed that the companion was well matched to low-gravity, L0–L1 spectral templates and free-floating substellar objects, with an implied mass of 13^{+12}_{-2} $M_{\rm Jup}$. The SED modeling of κ And b over a wide wavelength range and incorporating both near-IR spectroscopy and photometry allows us to revisit estimates of its temperature, better constrain its atmospheric properties (e.g., clouds), and potentially quantify its surface gravity.

Characterizing κ And b may provide broader insights into the nature of a new class of directly imaged companions. The estimated semimajor axis of κ And b (∼55–125 au) places it at a separation where formation by core accretion is difficult, yet its orbital inclination may imply formation in a disk, perhaps by disk instability (Currie et al. 2018). Other recent high-contrast imaging studies have also reported substellar-mass companions at these separations around B- and early A-type stars with masses nominally above the deuterium-burning limit (e.g., HIP 64892 and HIP 79098; Cheetham et al. 2018; Janson et al. 2019) and below it (HIP 65426; Chauvin et al. 2017). In addition to atmospheric characterization, improved orbital measurements of κ And b could better constrain its eccentricity, semimajor axis, and alignment with the star's rotation axis.

Here we aim at updating characterizations of the κ And system by using Subaru/HiCIAO+SCExAO and Keck/NIRC2 (Section 2). By expanding wavelength coverage for κ And b, we perform a more robust comparison with other substellar objects and synthetic atmospheric models, allowing us to better constrain the companion's temperature and gravity and infer its cloud properties (Sections 3 and 4). Additionally, we expand the planet's astrometric coverage, adding two additional epochs to update an estimate of its orbital properties (Section 5). We discuss possible formation and evolution scenarios accounting for κ And b's properties in Section 6.

2. Data

2.1. Observations

2.1.1. Subaru/SCExAO+HiCIAO

On UT 2016 July 18, κ Andromedae was observed with SCExAO coupled to the HiCIAO infrared camera operating in the Maunakea H (λ = 1.49–1.78 μm) and Y (0.957–1.120 μm) broadband filters (Table 2) with a pixel scale of 0.″0083 pixel^{-1}. Conditions were photometric and slightly above average in quality for Maunakea: visual seeing of 0.″4–0.″5, negligible humidity, and light winds (2 m s^{-1}).

In both filters, science frames consisted of 30 s coadded exposures (six coadds of 5 s individual frames). As we did not use a coronagraph in either case, the primary star halo is saturated out to $\rho \sim$ 0.″2–0.″25 and 0.″15–0.″2 in the H and Y bands, respectively. We also took unsaturated images in both bands for point-spread function (PSF) reference with 5 s integration time and the ND0.1 filter. The measured FWHM in both sets of unsaturated frames is 5.2 pixels in the H band and 6.2 pixels in the Y band.

We utilized angular differential imaging (ADI; Marois et al. 2006) to achieve high enough contrast to detect fainter objects around the central star, yielding significantly. Our field rotation due to ADI (∼41°–42°) is larger and integration time ($t_{\rm int}$ ∼ 25–30 minutes) is greater than the higher-quality SCExAO/CHARIS data presented in Currie et al. (2018; 10.°5 rotation, 14.4 minutes of integration time).

The transmission of each ND0.1 filter was measured after the observations to be 0.0085% ± 0.0006% in the Y band and 0.063% ± 0.020% in the H band. We found that the H-band ND0.1 filter has a large uncertainty; thus, we cannot conduct accurate relative photometry using κ And A. Therefore, we alternatively used unsaturated images of HIP 79977, which were taken in the same epoch with the H-band ND1 filter (0.854% ± 0.002%), as a photometric reference. For the Y band, because κ And A lacks published precise Y-band photometry, we also took unsaturated frames of HIP 118133 as a photometric reference, with 5 s integration time and the Y-band ND1 filter (0.388% ± 0.008%). Detailed discussions of photometry are given in Section 2.3.

We also took advantages of an SCExAO engineering data set taken on 2015 August 2. The inaccurate ND0.1 filter was also mainly used for unsaturated frames of κ And in this epoch, and we used one unsaturated frame, with which the H-band ND1 filter was used, for a photometric reference. Furthermore, this epoch did not take a globular cluster or binary system for

Table 2
Observing Logs for κ And

Date (*HST*)	Instrument	Band	T_{exp} (minutes)	Rotation Angle (deg)	Remarks
2015 Aug 2	Subaru/HiCIAO+SCExAO	*H*	35.0	27.70	SCExAO engineering obs.
2016 Jul 18	Subaru/HiCIAO+SCExAO	*H*	25.0	41.70	Science obs.
2016 Jul 18	Subaru/HiCIAO+SCExAO	*Y*	30.5	41.31	Science obs. for photometry
2018 Nov 1	Keck/NIRC2	K_s	10	3.70	Science obs. for astrometry

distortion correction, which yields a systematic astrometry offset. Although we report our results of photometry and astrometry, we do not use the astrometric result of this engineering run for the discussion hereafter.

2.1.2. Keck/NIRC2

To add new constraints on κ And b's orbit, we obtained follow-up observations of κ And with Keck/NIRC2 in the K_s band ($\lambda = 1.99$–2.30 μm filter using the Lyot coronagraph with a 400 mas occulting spot).

2.2. Data Reduction

Basic imaging processing—e.g., flat-fielding, dark subtraction, bad-pixel masking, distortion correction, and precise PSF registration—followed previous methods taken for SCExAO/HiCIAO data (Currie et al. 2017; Garcia et al. 2017). In the distortion correction, we used a master distortion map of SCExAO+HiCIAO, which was made by observing a globular cluster of M15 (Currie et al. 2017). Registered images were visually inspected to identify a few with poorer AO correction and/or data transfer errors from HiCIAO (e.g., sporadic NaN stripes in one or two channels).

For PSF subtraction of the HiCIAO data sets, we used a slightly modified version of the locally optimized combination of images (LOCI) pipeline (Lafrenière et al. 2007), inverting the covariance matrix in LOCI using a truncated singular value decomposition (SVD), as in A-LOCI (Currie et al. 2012a, 2019b). As κ And b is visible in the raw *H*-band data, we opted for conservative settings for both filters: a rotation gap of 0.75 λ/D, an optimization zone from which we constructed a weighted reference PSF of 300 PSF footprints, and a light SVD cutoff of 10^{-7}.

For the Keck/NIRC2 coronagraphic data, basic image processing followed previous methods (e.g., Currie et al. 2012b). Briefly, after applying corrections for linearity, dark subtraction, and flat-fielding, we registered the images to a common center using the stellar PSF seen through the partially transmissive mask. For PSF subtraction, we used A-LOCI with local masking and an SVD cutoff of 10^{-6}.

Our data reduction detected κ And b with S/Ns of $\sim$10 in the *Y* band and $\sim$130 in the *H* band (see Figure 1) for the 2016 SCExAO+HiCIAO data sets and S/N $\sim$ 14 in the Keck/NIRC2 data. We also detected κ And b with an S/N of >80 in the 2015 engineering data (see Figure 2). Compared to Carson et al. (2013), who measured an S/N $\sim$ 20–25 in the *H* band with the Subaru/HiCIAO+AO188, our *H*-band data yielded higher-S/N detections. Hinkley et al. (2013) used Project 1604/Palomar integral field spectroscopy to extract κ And b's spectrum in the *YJH* bands. Over the five channels encompassing the *Y* band, the mean ratio of their flux-to-flux uncertainty is $\sim$3, where uncertainties are drawn from the local properties of the noise. Assuming no contribution from systematic uncertainties and an S/N gain from median-combining channels scaling with the square root of the number of channels, their band-integrated S/N should be $\sim$6.5 or less. Thus, our *Y*-band data likely detect κ And b at a higher S/N. The *H*-band detections are comparable in significance to that achieved with high-quality SCExAO+CHARIS data from Currie et al. (2018) due to our data's greater depth and field rotation.

We also calculated contrast limits for κ And data sets (see Figure 3). We convolved the final images, which were normalized with exposure times, and extracted noise profiles from them. Figure 3 shows the calculated 5σ contrast limits of SCExAO+HiCIAO observations. The *H* band achieved a better contrast level than the *Y*-band observation; the 5σ contrast limit is 1.5×10^{-4}, 2.8×10^{-5}, and 2.7×10^{-6} at 0.″25, 0.″5, and 1″, respectively. At $\rho \sim 0.''3$–$0.''75$, the planet-to-star contrasts for the SCExAO/CHARIS broadband data in Currie et al. (2018) are about a factor of 2–5 better than those reported here for SCExAO/HiCIAO at the *H* band due to the CHARIS data's better PSF quality and utilization of ADI+SDI for PSF subtraction. Similarly, the SCExAO/HiCIAO *H*-band contrasts in Kühn et al. (2018), which were taken on a different date, 2016 November 12 UT, are typically a factor of 2 deeper, likely due to usage of the vector vortex coronagraph.

2.3. Photometry and Astrometry

We used aperture photometry for measuring photometry and PSF fitting for estimating FWHM and astrometry in this section. For absolute photometric calibration, we primarily relied on unsaturated images of other stars obtained through well-calibrated neutral density filters. As a photometric reference of the *Y*-band image to calibrate both κ And A and κ And b, HIP 118133 (*Y*-band magnitude of 6.60 ± 0.06 mag; Pickles & Depagne 2010) was used. HIP 118133 was observed immediately after κ And and at a comparable airmass.[20] The implied *Y*-band photometry for κ And A (4.28 ± 0.09) is consistent with the primary having (near-)zero infrared colors, as expected for a B9V star (e.g., Currie et al. 2010; Pecaut & Mamajek 2013).

We also checked our *H*-band photometric results. Although unsaturated frames of κ And in the *H* band were taken at both epochs (2015 and 2016), those data used the ND0.1 filter, which was reported to have a high uncertainty in its transmission efficiency. Therefore, we used another set of unsaturated images of HIP 79977, which has an *H*-band magnitude of 7.854 ± 0.03 mag (2MASS; Cutri et al. 2003), for the *H*-band photometric reference. In the engineering run,

[20] The difference in AO performance between HIP 118133 and κ And was insignificant for the purposes of photometric calibration (see also Currie et al. 2019a).

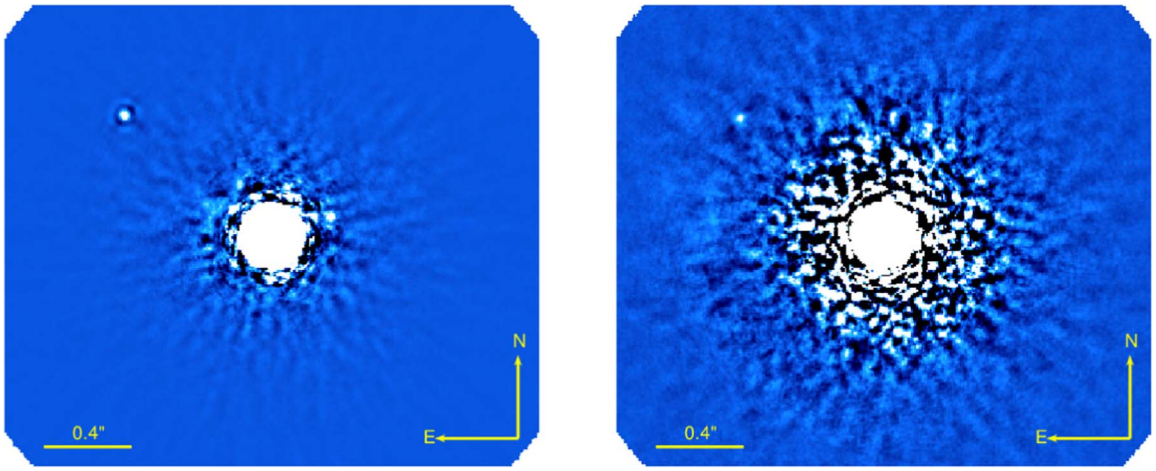

Figure 1. The ADI-reduced κ And data sets taken by Subaru/SCExAO+HiCIAO in the *H* band (left) and *Y* band (right) in 2016. The central star is masked, and the companion is detected in all images. North is up, and east is left.

the ND1 filter was used to take one unsaturated frame, and we used this image as the photometric reference.

To estimate the throughput correction for κ And b needed to compensate for signal loss due to PSF subtraction, as well as the astrometric biasing, we injected synthetic companions that are made from an unsaturated PSF of the central star observed through the neutral density filter in each bandpass or (for Keck) with an intensity distribution approximating the star as seen through the partially transmissive coronagraph mask. In the *H* and K_s bands, we calculated the throughput correction and astrometric biasing over a FWHM-wide area. In the *Y* band, we adopted a smaller aperture (4.4 pixels or 37 mas), corresponding to most of the PSF core and the apparent PSF size of the real κ And b. To confirm the reliability of our PSF model at the *Y* band, we verified that the FWHM of the partially annealed synthetic planet PSF matches that of the real κ And b. The signal throughput in each case is high—above 80% for all data sets and ~90% for the Keck/NIRC2 data.

Table 3 shows our photometric results for the κ And system. Our *H*-band photometry agrees with that derived from SCExAO/CHARIS ($H = 15.01 \pm 0.07$; Currie et al. 2018) and earlier AO188/HiCIAO photometry from Bonnefoy et al. (2014b; $H = 14.95 \pm 0.13$). Because the photometric uncertainty with our data is higher than that with the SCExAO/CHARIS results, we use only our *Y*-band result to update the photometric parameters of κ And b for atmospheric analysis. Table 4 summarizes photometric results of κ And b. The *H*-band data are used for astrometric analysis. Table 5 summarizes the astrometric results of our data sets, as well as previous studies.[21] As mentioned above, we calculated astrometric biases when we estimated throughputs by injecting fake sources, which is included in the errors. The major contributors for the astrometric errors are the intrinsic S/N of the detection and the uncertainty in the centroid position. In case of the Keck data set, we have 0.″003 errors in *x*- and *y*-position measurement of κ And b and half a pixel uncertainties of in the centroid measurement, which resulted in 0.″006 errors in Table 5. The centroid was measured by using the PSF seen underneath the partially transmissible coronagraph mask, which gave a better S/N for κ And b than estimating the centroid using the halo outside the mask. Orbital fitting using these results is described in Section 5.

[21] The 2015 HiCIAO data provided (ΔR.A., ΔDecl.) = ($0.767 \pm$??, $0.638 \pm$??). We have unknown systematic errors due to no distortion correction applied in the SCExAO engineering data. This data set is not presented in Table 5.

3. Empirical Comparisons to κ And b's Photometry and Spectra

We add κ And b's *Y*-band photometry to CHARIS *JHK* spectra to provide a new empirical context for the companion's near-infrared properties. Previous empirical spectral analysis from Currie et al. (2018) using spectral templates and a homogeneously reduced library of substellar object spectra pointed toward κ And b being an L0–L1 low surface gravity object consistent with a young, planet-mass companion. Our new data extend the available wavelength baseline for κ And b data. We compare κ And b's broadband photometry to field and low-gravity objects using a larger set of empirical substellar object spectra.

3.1. Near-infrared Colors

We first investigated a color–magnitude diagram of κ And b by comparing it to other low-mass objects with precise parallaxes and various gravities reported in Liu et al. (2016). The Liu et al. (2016) sample includes 67 MLT dwarfs with new, precise parallaxes and another 35 with literature parallaxes and near-infrared photometry. Drawing from the Liu et al. (2016) polynomial fits for absolute magnitudes versus spectral for different gravity classes, we constructed linear fits to magnitudes and colors in $Y/Y-K$ space.

Figure 4 shows how κ And b's color–magnitude diagram position fits within the context of other substellar objects. The companion appears redder than a typical field-gravity L object (red), in between these colors and those for a typical low-gravity L object (yellow) at its *Y*-band luminosity. Moreover, its location appears on the locus (gray dashed line) connecting the L2 field and low surface gravity objects. The uncertainty of the $Y-K$ color of κ And b and the amplitude of the scatter of objects about the polynomial fits from Liu et al. (2016) preclude us from excluding a high- or low-gravity scenario at a significant level using only the *Y*- and *K*-band luminosities.

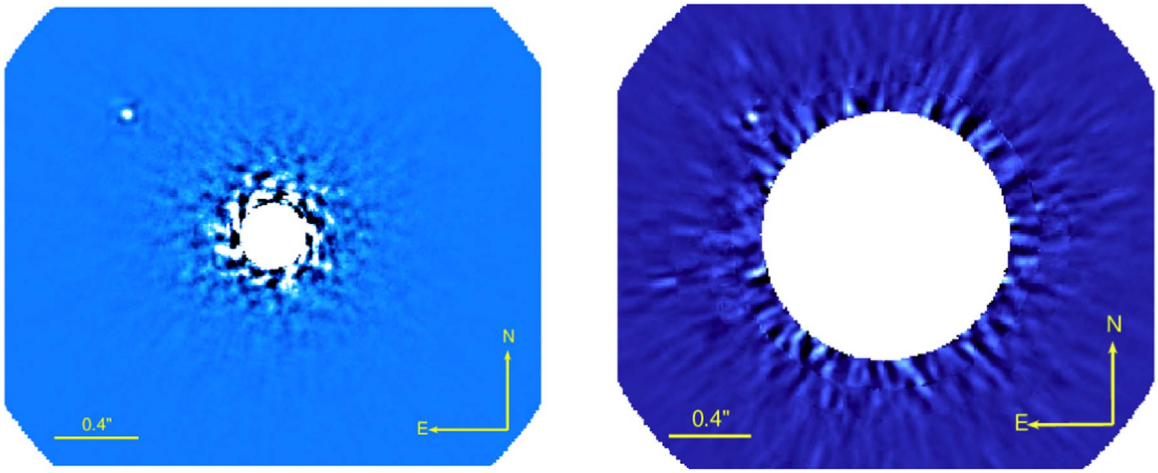

Figure 2. Same as Figure 1 but for the SCExAO engineering run taken in 2015 (left) and Keck/NIRC2 (right).

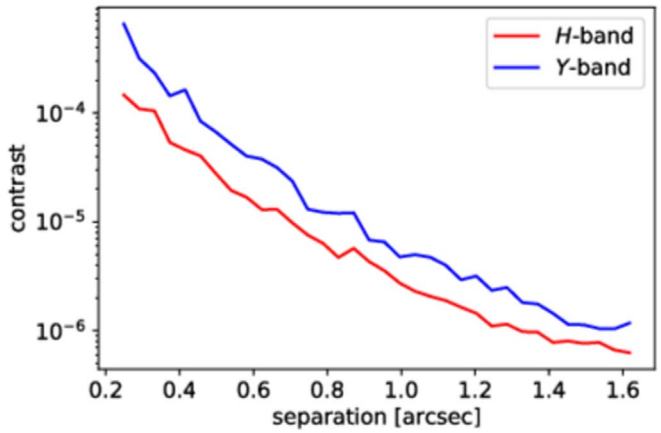

Figure 3. The 5σ contrast limits of SCExAO+HiCIAO observations taken in 2016.

Table 3
Photometric Results of Our Work

Band	κ And A (mag)	κ And b (mag)
H	⋯	15.18 ± 0.56[a]
Y	4.28 ± 0.09	17.04 ± 0.15

Note.
[a] Large uncertainty that can be related to the unknown offset of the engineering run and different photometric reference in the 2016 data.

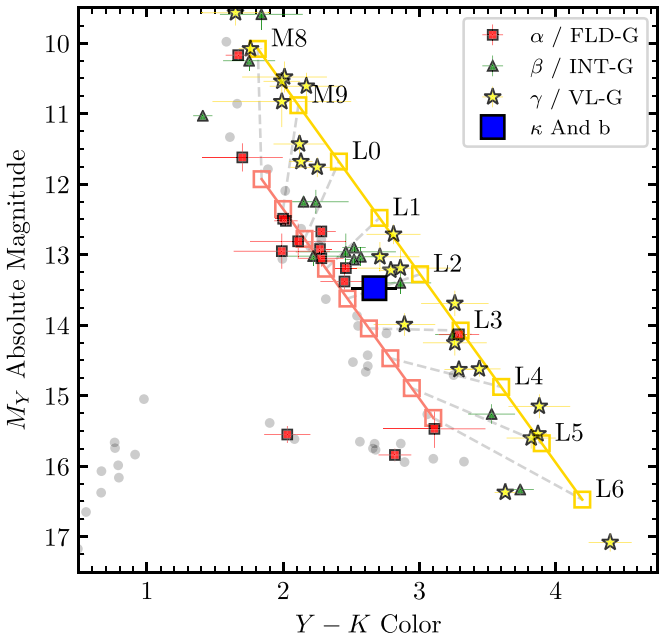

Figure 4. Near-infrared color–magnitude diagram showing κ And b (blue square) relative to other substellar objects with trigonometric parallax measurements from Liu et al. (2016). Objects without a literature gravity classification are denoted by small gray circles. Linear fits to the absolute magnitude and colors of field gravity (red open squares) and low gravity (yellow open squares) are also shown. Here κ And b appears somewhat redder than field-gravity objects with a similar Y-band absolute magnitude, but not at a significant level.

Second, we use a large sample of substellar objects with different spectral types and gravity classifications to provide a context for κ And b's near-infrared colors. We compiled a library of 2011 M-, L-, and T-dwarf spectra drawn from the SpeX Prism library[22] (Burgasser 2014), IRTF Spectral Library[23] (Cushing et al. 2005), Montreal Spectral Library[24] (e.g., Gagné et al. 2015; Robert et al. 2016), and the sample of young ultracool dwarfs presented in Allers & Liu (2013). We do not incorporate the library of young, low-gravity objects presented in Bonnefoy et al. (2014a) and used by Currie et al. (2018) in their analysis of κ And b, as the SINFONI spectra do not extend into the Y band and thus cannot be compared to the new photometry presented in this work. The spectral types were obtained from a number of literature source and are given for a number of sources highlighted in the remainder of this section. We preferentially used the near-infrared spectral type if both an optical and a near-infrared classification were available. Gravity classifications for a subset of the objects were also obtained from the literature, using either of the schemes outlined by Kirkpatrick (2005), Kirkpatrick et al. (2006), Cruz et al. (2009; α, β, γ, δ in descending order of surface gravity), or Allers & Liu (2013; FLD-G, INT-G, VL-G, similarly). Both of these classification schemes share three categories: surface gravity indicators consistent with those observed in old field dwarfs (α, FLD-G), intermediate surface gravity (β, INT-G), and

[22] http://pono.ucsd.edu/~adam/browndwarfs/spexprism/
[23] http://irtfweb.ifa.hawaii.edu/~spex/IRTF_Spectral_Library/
[24] https://jgagneastro.wordpress.com/the-montreal-spectral-library/

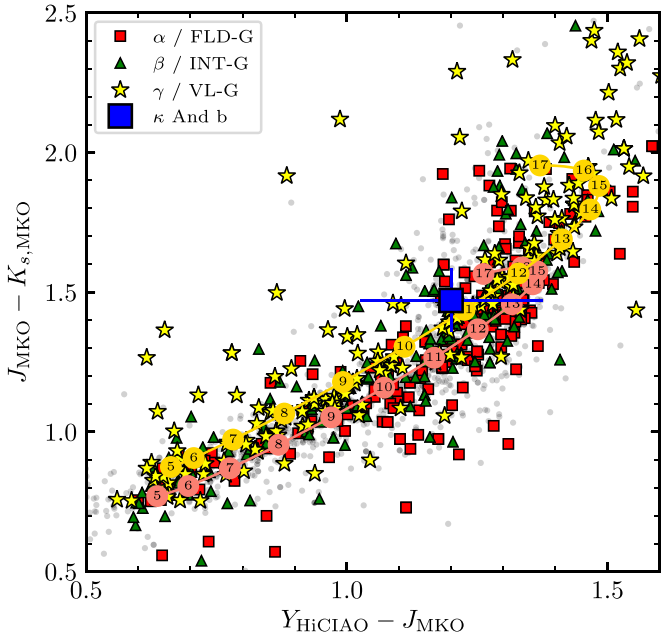

Figure 5. Near-infrared color–color diagram magnitude diagram showing κ And b (blue square with error bars) compared to $Y - J$ and $J - K$ colors for objects in our spectral library. Third-order polynomial fits to the color as a function of spectral type are plotted as red (field gravity) and yellow (very low gravity) lines, with M0 = 0, L0 = 10, etc. Red squares, green triangles, and yellow stars denote objects with field, intermediate gravity/β and very low gravity/γ, respectively. Gray dots denote dwarfs without gravity classifications.

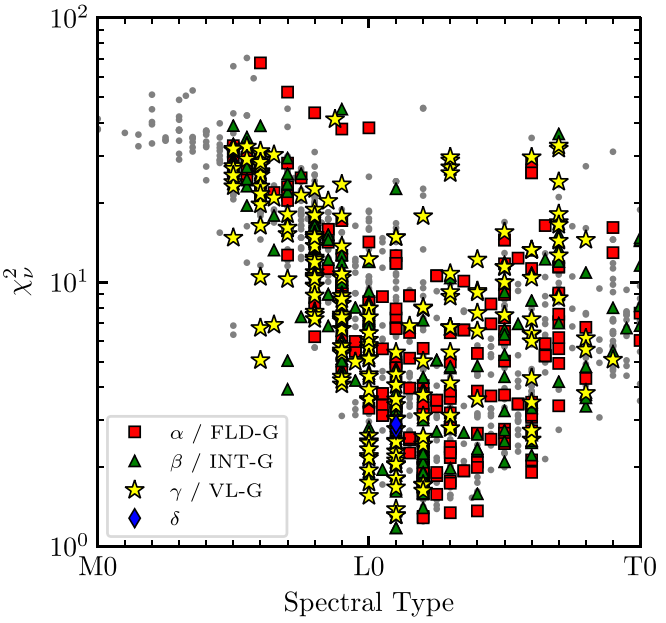

Figure 6. Goodness of fit as a function of spectral types for the objects within the spectral library compared to the near-infrared photometry and low-resolution spectroscopy of κ And b. Comparison objects with previously published gravity classifications in the literature are highlighted. Our analysis shows that some objects with low χ^2 that are either unclassified or were previously classified as field dwarfs/intermediate-gravity dwarfs may in fact be low-gravity objects (see the text). Blue diamonds denote δ gravities.

a very low surface gravity observed for substellar objects in nearby young moving groups (γ, VL-G). The fourth classification, δ, was defined by Kirkpatrick (2005) for objects that exhibit stronger gravity-sensitive features than seen for those classified as γ/VL-G.

We computed synthetic Y_{HiCIAO}, J_{MKO}, H_{MKO}, and $K_{s,MKO}$ photometry for the library by convolving the spectra with the appropriate filter response curves given in Figure 14 and Tokunaga et al. (2002). Figure 5 compares κ And b's $Y - J$ and $J - K$ colors to library objects with different gravity classifications. The main locus of library colors extends from $Y - J/J - K \sim 0.6/0.8$ to $1.3/1.5$ for M5 to L3 dwarfs. Young objects with intermediate or (very) low gravity appear systematically redder in $J - K$, as expected from previous studies (Liu et al. 2016). The position of κ And b lies between typical L0 and L2 colors, above the positions for most field objects and overlapping with younger, lower-gravity objects.

3.2. *Joint* Y*-band photometry and CHARIS* JHK *Spectral Comparisons*

To assess the overall best-fitting objects among the libraries, we fit κ And b's Y-band photometry and CHARIS spectra. Library spectra were convolved and interpolated to CHARIS's wavelengths and spectral resolution, assuming a constant resolution of $R = 20$ across the full spectrum. We removed 20 library spectra that did not have wavelength coverage spanning the Y through K bands. A small subset of the library had H-band spectra that were truncated at $\sim$1.75 μm, shorter than the reddest H-band channel in the CHARIS spectrum at 1.8 μm. For these 135 spectra, we excluded this CHARIS channel from the fit and reduced the number of degrees of freedom by one when calculating χ^2_ν.

We computed the goodness of fit for each object by calculating χ^2_{spec} from a comparison of the κ And b spectrum to the smoothed library spectra using the correlation matrix given in Currie et al. (2018) and χ^2_{phot} from a comparison of the near-infrared photometry of κ And b to the synthetic photometry of the objects within the library. As we were primarily interested in comparing the spectral morphology of κ And b to the objects within the library, we computed the scaling factor to apply to the library spectrum and photometry that minimized $\chi^2 = \chi^2_{spec} + \chi^2_{phot}$. We did not incorporate the library spectra measurement uncertainty; these were typically negligible when convolved to CHARIS's resolution.

Figure 6 displays the χ^2_ν distribution for M0–T0 objects in the library. Early L-type objects show a clear minimum, consistent with analyses presented in Bonnefoy et al. (2014b) and Currie et al. (2018). The exact location of the minimum differs for field and low-gravity objects; at L1 for γ/VL-G objects and L2–L3 for α/FLD objects, a consequence of the redder near-infrared colors of low-gravity objects is compared to field objects of the same spectral type (e.g., Liu et al. 2016, Figure 15). This effect is also seen when comparing κ And b to the L-type standards proposed by Cruz et al. (2018), shown in Figure 7, where the best-fit low-gravity standard is L1 ($\chi^2_\nu = 1.8$) and later spectral types (L3–L4) fit far worse, while the best-fit field-gravity standards are L2–L3 and earlier spectral types (e.g., L0) fit far more poorly. This trend is consistent with that seen for synthetic spectral templates (composites of individual spectral standards for a given spectral type/gravity class; Cruz et al. 2018) in Currie et al. (2018): they found that the best-fit low-gravity template (L0$_\gamma$; $\chi^2_\nu \sim 1.26$) is three subtypes earlier than the best-fit field-gravity template (L3; $\chi^2_\nu \sim 1.51$).

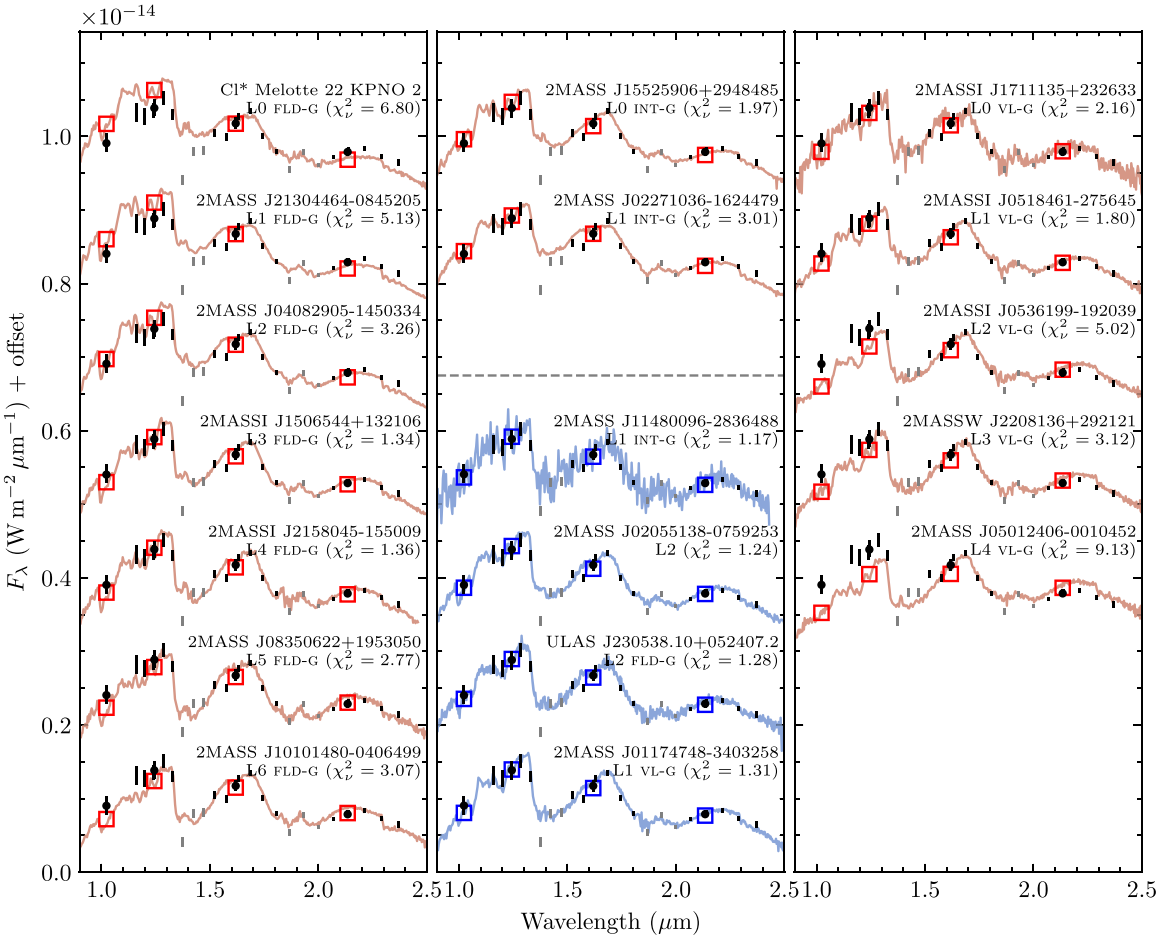

Figure 7. Near-infrared SED of κ And b (black points) compared to the early L-type near-infrared standards proposed by Cruz et al. (2018) for field (L0–L6α; left panel), intermediate (L0–L1β; middle panel), and very low (L0–L4γ; right panel) surface gravities (red). CHARIS spectral channels within the water absorption bands were not included in the fit (gray points). Four of the best-fit objects within the complete library are also plotted in the middle panel (blue). Their previously published gravity classifications are given; our analysis revises some of them to lower gravity classes. Spectra are from Burgasser & McElwain (2006), Chiu et al. (2006), Reid et al. (2006), Burgasser (2007), Burgasser et al.(2008, 2010), Kirkpatrick et al. (2010), Allers & Liu (2013), Bardalez Gagliuffi et al. (2014), Filippazzo et al. (2015), Gagné et al. (2015), Kellogg et al. (2017), and Cruz et al. (2018).

Of the objects within the complete library, the best fit was 2MASS J11480096–2836488 ($\chi^2_\nu = 1.2$), previously classified as an L1 intermediate-gravity member of the 10 Myr (Bell et al. 2015) TWA moving group (Gagné et al. 2015, 2018) and an isochronal mass of $\sim$8 $M_{\rm Jup}$ (Gagné et al. 2015). While the S/N of the spectrum for this object is lower than the typical library spectrum, the uncertainties are comparable to those of the spectrum of κ And b when degraded to the same resolution. Good fits were also found to 2MASS J01174748–3403258 ($\chi^2_\nu = 1.3$; previously classified as L1 γ) and to 2MASS J02055138–0759253 and ULAS J230538.10+052407.2 ($\chi^2_\nu =$ 1.2 and 1.3), which previously were unclassified or classified as being field-gravity L2 dwarfs. In total, 36 objects have a $\chi^2_\nu < 1.7$ (95% confidence level) with the following previous classifications: one L0 (VL-G), five L1 (two INT-G, three VL-G), 22 L2 (11 without classification, eight FLD-G, two INT-G, one VL-G), four L3 (three without classification, one FLD-G), and four L4 (two without classification, one FLD-G, and one INT-G). For reference, the complete library contains 656 objects between L0 and L4: 381 without classification, 112 FLD-G, 80 INT-G, and 81 VL-G.

To further investigate the nature of the four best-fit objects, we separately estimated spectral types using the derived gravity classifications following the spectral index–based methods in Allers & Liu (2013): i.e., the H_2O, H_2O-1, H_2O-2, and H_2O-D indices for spectral typing and Fe_z, VO, KI_J, and $H_{\rm cont}$ for gravity scoring. We nominally box-car smooth the spectrum using a window size of three spectral channels and explore the results obtained with different windows. Our analysis recovers the previous classification for 2MASS J01174748–3403258 (L1 γ). However, it favors reclassifying 2MASS J02055138–0759253 and ULAS J230538.10+052407.2 as L2 β objects (gravity scores 1111 and 1120), respectively; Banyan-Σ suggests that 2MASS J02055138–0759253's kinematics may be consistent with membership in the 40 Myr old Columba association, depending on its parallax. Given the noisiness of 2MASS J01174748–3403258's spectrum, we cannot derive a gravity score from Fe_z, VO, and KI_J. However, its $H_{\rm cont}$ index (1.05 ± 0.05) suggests a low gravity and possible reclassification to L1 γ. It is likely that the other well-fitting objects previously given a field classification or no classification at all are in fact low-gravity objects.

To investigate the constraining power of our new *Y*-band photometry, we compared the χ^2 for each object with and without this measurement. For objects between L0 and L1, we typically find a larger $\Delta\chi^2$ for field-gravity objects (median $\Delta\chi^2$ of 4.1 compared to 1.2), indicating that the *Y*-band photometry is more consistent with that of a low-gravity object

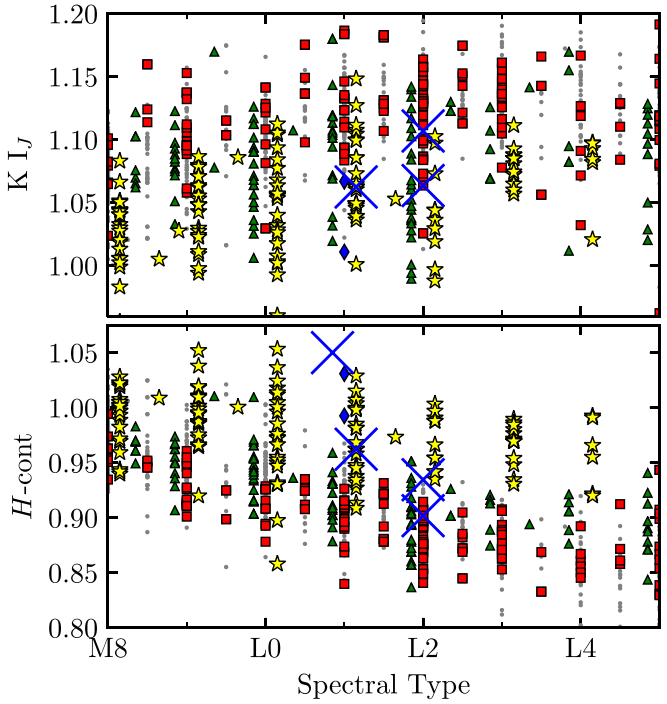

Figure 8. Surface gravity indicators from Allers & Liu (2013) as a function of spectral type for the objects within the spectral library. Symbols are the same as in Figure 6, with the four best-fit objects to the spectrum and photometry of κ And b highlighted with blue crosses (the spectrum of 2MASS J1148 is too noisy for a reliable estimate of its KI_J index). The spectral types of intermediate- and low-gravity objects have been displaced slightly (±0.15 subtypes) for clarity.

over this range of spectral types. For later spectral types, this is reversed, with $\Delta\chi^2$ typically being larger for low-gravity objects between L2 and L5 (median $\Delta\chi^2$ of 6.9 compared to 0.7). This is a consequence of the red color of low-gravity objects; an object with a given Y-band flux (or $Y-J$ color) either has lower gravity and an earlier spectral type or higher gravity and a later spectral type.

Preference for a low surface gravity for κ And b can also be inferred using the gravity-sensitive spectral indices defined by Allers & Liu (2013). While these indices cannot be computed directly given the low resolution of the spectrum, they can be computed for the objects within the library with the most similar spectra to κ And b. Two of these indices are plotted in Figure 8, showing that the best-fit objects are more consistent with the population of low-gravity objects and (some) intermediate-gravity objects than the median of the field-gravity sequence.

4. Comparison with Model Atmospheres

The CHARIS near-infrared spectrum from Currie et al. (2018), the Y-band photometry presented in this work, and the literature photometry spanning 1.2–4.7 μm (Table 4) were fit to a number of models of substellar atmospheres. These model grids can be broadly categorized into those that incorporate a prescription for the formation of clouds within the photosphere and those that enforce a clear photosphere over the full range of effective temperatures and surface gravities. The first group contains the AMES-Cond (Allard et al. 2001), BT-Cond (Allard et al. 2012), and Burrows et al. (2006) model grids. The AMES-COND and BT-COND grids both use the same PHOENIX atmosphere code (Hauschildt 1992) but different molecular line lists (Partridge & Schwenke 1997 and Barber et al. 2006, respectively). These two grids ignored dust opacity entirely in order to simulate the immediate sedimentation of dust into the lower atmosphere leading to a clear photosphere. The Burrows et al. (2006) clear atmosphere grid was created using the TLUSTY atmosphere code (Hubeny & Lanz 1995), similarly ignoring opacity from condensates within the photosphere.

Table 4
Summary of Photometry of κ And System

Band	κ And A	κ And b	Reference
Y [mag]	4.28 ± 0.09	17.04 ± 0.15	(1)
J [mag]	4.26 ± 0.04	15.84 ± 0.09	(2)
H [mag]	4.31 ± 0.05	15.01 ± 0.07	(2)
K_s [mag]	4.32 ± 0.05	14.37 ± 0.07	(2)
L' [mag]	4.32 ± 0.05	13.12 ± 0.1	(3), (4)
$NB\_4.05$ [mag]	4.32 ± 0.05	13.0 ± 0.2	(4)
M' [mag]	4.30 ± 0.06	13.3 ± 0.3	(4)

References. (1) This work. (2) Currie et al. (2018). (3) Carson et al. (2013). (4) Bonnefoy et al. (2014b).

The second group contains a number of different treatments for photospheric clouds. The AMES-Dusty (Allard et al. 2001) and BT-Dusty (Allard et al. 2012) grids were created using the same atmospheric code and line lists as the clear photosphere models described previously but instead including dust opacity in the calculation of the emergent spectra and neglecting gravitational sedimentation entirely. The various BT-Settl grids (Allard et al. 2012) were also calculated with the same code but with a revised treatment for dust sedimentation to better model the L/T transition from cloudy to clear photospheres. The Drift-Phoenix grid (Witte et al. 2011) used the same PHOENIX code but a completely revised treatment for the formation and evolution of photospheric clouds that reproduces the observed SED of young, low-gravity objects (e.g., Patience et al. 2012; Lachapelle et al. 2015). The Burrows et al. (2006) models simulate clouds of a variety of condensates as extending between the scale heights set by the most and least refractory condensates, with an exponential decay above and below. The extent of the clouds and the size distribution of particles within the clouds are free parameters within the model. Here we compare to the fiducial cloud model used in Burrows et al. (2006) that has a model particle size of 100 μm, as well as to the thick cloud models with smaller modal particle sizes (4 and 10 μm) used in Currie et al. (2014a). A summary of the various atmosphere model grids and their coverage and resolution in ($T_{\rm eff}$, $\log g$) space is given in Table 6.

The model atmospheres were fit to the observed photometry and spectroscopy of κ And b using a similar procedure as for the empirical comparison described in Section 3.1, including the thermal infrared measurements given in Table 4. We applied a limit on the value of the dilution factor (r^2/d^2) such that the radius of the companion was between 0.5 and 3.0 $R_{\rm Jup}$, encompassing the range of radii predicted for young substellar companions (e.g., Fortney et al. 2008). As with Currie et al. (2018), we assume a distance of $d = 50.0$ pc (Table 1; Gaia Collaboration et al. 2018). The best-fit model and corresponding χ^2 within each grid are given in Table 6.

Cloudy models are preferred by a significant margin, although the quality of the fit varies between each grid. Of all the models tested, the best fit was the 1700 K, $\log g = 4.0$ [dex] model within

Table 5
κ And b's Relative Locations

Date (UT)	Instrument	ΔR.A. [arcsec]	ΔDecl. [arcsec]	Reference
2012 Jan 1	Subaru/AO188+HiCIAO	0.884 ± 0.010	0.603 ± 0.011	(1)
2012 Jul 8	Subaru/AO188+HiCIAO	0.877 ± 0.007	0.592 ± 0.007	(1)
2012 Nov 3	Keck/NIRC2	0.846 ± 0.010	0.584 ± 0.010	(2), (3)
2013 Aug 18	Keck/NIRC2	0.829 ± 0.010	0.585 ± 0.010	(2)
2016 Jul 18	Subaru/SCExAO+HiCIAO	0.734 ± 0.008	0.599 ± 0.007	(4)
2017 Sep 5	Subaru/SCExAO+CHARIS	0.710 ± 0.016	0.576 ± 0.012	(2)
2017 Dec 9	Keck/NIRC2	0.699 ± 0.010	0.581 ± 0.010	(2)
2018 Nov 1	Keck/NIRC2	0.656 ± 0.006	0.580 ± 0.006	(4)

References. (1) Carson et al. (2013). (2) Currie et al. (2018). (3) Bonnefoy et al. (2014b). (4) This work.

the DRIFT-PHOENIX grid. This model is plotted against the SED of κ And b in Figure 9, alongside the two other best-fitting models from the BT-SETTL and BT-DUSTY grids. The temperatures of these models are consistent with the spectral type determined previously. The Burrows model fitting results favor thick clouds and a modal dust size somewhere between 4 and 100 μm.

Two of the grids displayed in Figure 9—DRIFT-PHOENIX and BT-DUSTY—suggest a low surface gravity consistent with our empirical comparisons. The BT-DUSTY grid only covers a limited range of $\log g$, and the best fit was found at the grid boundary of $\log g = 4.5$ [dex]. Thus, it is likely that a BT-DUSTY model grid covering a wider range in gravity (e.g., $\log(g) = 3$–5) would result in a surface gravity approaching that found for DRIFT-PHOENIX ($\log g = 4.0$ [dex]). The best-fit model within the the third grid (BT-SETTL) has a similar goodness of fit but a higher surface gravity ($\log g = 5.0$ [dex]). The range of best-fit surface gravities for the three model grids is a reasonable proxy for the model uncertainty, demonstrating both how differences in assumptions regarding cloud properties and extent can affect derived bulk properties and that the surface gravity of κ And b cannot be conclusively derived from the low-resolution spectroscopy and photometry used in this study.

We repeated this exercise on an interpolated version of each grid to search for a better fit with combinations of $T_{\rm eff}$ and $\log g$ not included within the original grid. We constructed a new grid of models with an arbitrarily small grid spacing of $\Delta T_{\rm eff} = 1$ K and $\Delta \log g = 0.01$ [dex]. Models were constructed by performing a bilinear interpolation of the logarithm of the flux calculated within the seven photometric bands listed in Table 4 and the 16 spectral channels of the CHARIS spectrum presented in Currie et al. (2018). We find a significantly reduced χ^2_ν of 1.2 (compared with 1.7 in the coarse grid) for the DRIFT-PHOENIX model at $T_{\rm eff} = 1739$ K and $\log g = 4.0$ [dex] (Figure 9, bottom panel). A similar reduction in χ^2 is seen for the other two grids. The χ^2 surface for the interpolated version of the three best-fitting grids is shown in Figure 10, showing the radius required to minimize the χ^2 given the distance of 50.0 pc (Table 1) and the credible regions derived from the $\Delta\chi^2$ (with no treatment for model uncertainties).

We find that the best-fit models are able to reproduce the observed SED and are consistent with one another over the *JHK* range. At shorter and longer wavelengths, where the uncertainties on the photometric measurements are larger, the models diverge slightly. The lower-gravity DRIFT-PHOENIX model significantly underpredicts the flux at Y while slightly overpredicting the flux at M'. The higher-gravity BT-SETTL model predicts a larger flux at Y, consistent with the measured flux, but significantly underpredicts the flux at L'. Due to the differences in treatment for cloud formation and sedimentation within these models, as well as revisions to opacity tables used to compute the emergent spectra, it is difficult to ascribe the differences between the best-fit models to a particular property or feature of the models. A future study that incorporates high-resolution spectroscopy and precision photometry between 1 and 5 μm in conjunction with a retrieval-based modeling approach will allow us to investigate the effect of the bulk (e.g., temperature, surface gravity, luminosity) and photospheric (e.g., cloud extent and vertical distribution, dust condensation and sedimentation) properties on the emergent spectra of this object.

Figure 11 shows how the best-fit radii and gravities derived from atmospheric modeling compare to predictions from luminosity evolution models for a given age and mass. The gray contours adopt κ And b's luminosity derived from Currie et al. (2018; $\log L/L_\odot = -3.81 \pm 0.05$) and an age range of 47 ± 30 Myr—similar to the age range derived from a CHARA radius measurement of the host star in Jones et al. (2016). As the best-fit gravity for the BT-DUSTY model is at the lower limit of the grid ($\log(g) \sim 4.5$), we display its point with a downward arrow; the DRIFT-PHOENIX and BT-DUSTY model parameters are shown with error bars corresponding to the 68% confidence interval.

The best-fitting model atmosphere fit, DRIFT-PHOENIX, implies a radius and gravity consistent with evolutionary model predictions for an age of $t \leqslant 40$ Myr, nominally yielding a mass of 10 $M_{\rm Jup}$ and less than 20 $M_{\rm Jup}$ considering the errors. The BT-DUSTY model implies a mass less than ~30–35 $M_{\rm Jup}$; its radius/gravity is inconsistent with evolutionary models but could be reconciled if the gravity is lower by 0.5 dex or the radius is smaller by 0.2 $R_{\rm Jup}$, either of which would imply a mass less than 20 $M_{\rm Jup}$. The best-fit BT-SETTL model's radius and gravity imply higher masses and far older ages that are consistent with the early analysis by Hinkley et al. (2013). However, the implied radii and gravities are inconsistent with predictions from the evolutionary tracks in Figure 11. They also imply ages significantly older than and thus inconsistent with the ages derived from κ And A's radius using CHARA interferometry (Jones et al. 2016).

5. Orbital Fitting

Astrometric monitoring of κ And b over 8 yr helps constrain the orbital motion of the κ And system. The relative positions

Table 6
Summary of Atmosphere Models

Name	Reference	Special Remark	Model Properties $T_{\rm eff}$ (K)	log g [dex]	$\Delta T_{\rm eff}$ (K)	Δlog g [dex]	Best Fit $T_{\rm eff}$ (K)	log g [dex]	R ($R_{\rm Jup}$)	χ^2_ν
			Clear Models							
AMES-Cond	(1)	⋯	1000–2400	2.5–6.0	100	0.5	2400	4.0	0.74	29.7
BT-Cond	(2)	⋯	1000–2200	4.0–5.5	100	0.5	2200	4.0	0.85	20.4
Burrows	(3)	⋯	1000–2000	4.5–5.5	100	0.5	2000	4.5	0.90	53.9
			Cloudy Models							
AMES-Dusty	(1)	⋯	1000–2500	3.5–6.0	100	0.5	1800	5.0	1.19	3.62
BT-Dusty	(2)	⋯	1000–2400	4.5–5.5	100	0.5	1800	4.5	1.64	1.81
BT-Settl	(2)	Asplund et al. (2009) abundances	1000–2400	3.0–5.5	100	0.5	1900	4.5	1.23	2.80
BT-Settl	(2)	Caffau et al. (2011) abundances	1000–2400	3.5–5.5	50	0.5	1800	5.0	1.34	1.70
BT-Settl-2015	(2)	⋯	1200–2400	3.0–5.5	50	0.5	1750	5.5	1.37	3.49
BT-Settl-bc	(2)	⋯	1100–2400	3.0–5.5	100	0.5	1800	4.0	1.30	2.99
Drift-Phoenix	(4)	⋯	1000–2400	3.0–6.0	100	0.5	1700	4.0	1.57	1.66
Burrows	(3)	Nominal cloud model, 100 μm modal size (E100)	1000–2000	4.5–5.5	50	0.1	1800	4.6	1.25	7.08
Burrows	(5)	Thick clouds, 4 μm modal size (A4)	1800–2200	3.5–4.0	25–100	0.25	1900	4.0	1.23	6.39
Burrows	(5)	Thick clouds, 10 μm modal size (A10)	1800–2200	3.6–4.0	100	0.1	2000	4.0	1.09	3.24

References. (1) Allard et al. (2001). (2) Allard et al. (2012). (3) Burrows et al. (2006). (4) Witte et al. (2011). (5) Currie et al. (2014a).

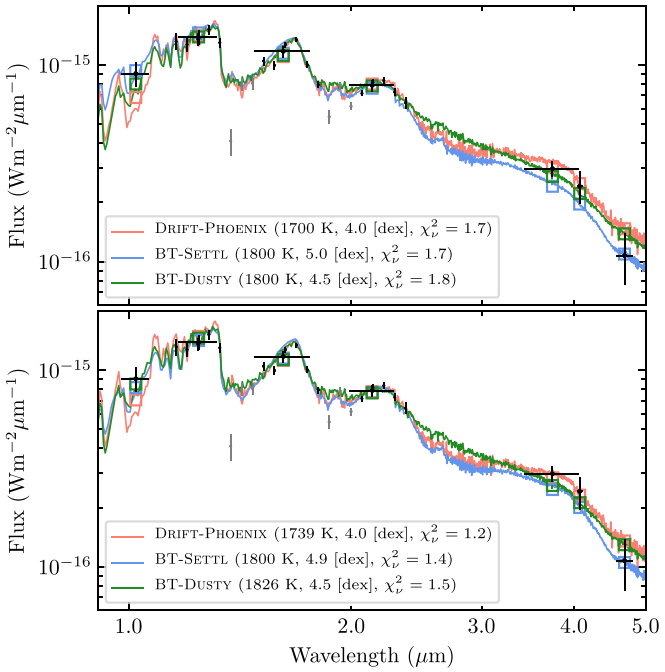

Figure 9. Best-fit model atmosphere within Drift-Phoenix (red), BT-Settl (blue), and BT-Dusty (green) to the observed SED of κ And b without (top) and with interpolation between the grid points of the models. The spectrophotometry of κ And b is overplotted (black), with the low-S/N channels of the CHARIS spectrum excluded from the fit shown in gray.

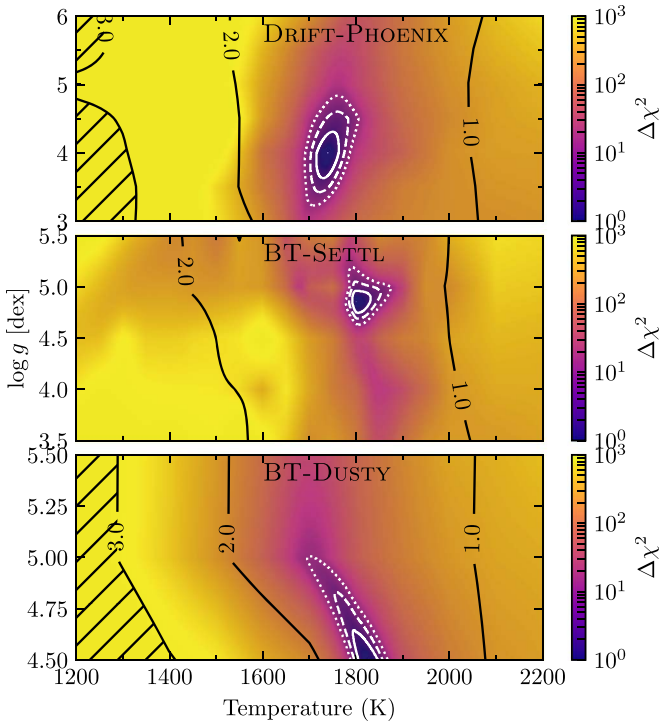

Figure 10. The $\Delta\chi^2$ surface for the Drift-Phoenix (top), BT-Settl (middle), and BT-Dusty (bottom) grids calculated using the interpolated version of each grid. Black contours denote the radius required to minimize the χ^2; hatched regions require a nonphysical radius of >3 $R_{\rm Jup}$. White contours denote 1σ, 2σ, and 3σ credible regions, computed from the $\Delta\chi^2$.

of κ And b obtained by Subaru/Keck observations are summarized in Table 5. Blunt et al. (2017) estimated the orbital parameters of κ And b from only three relative positions from 2011 to 2012 (Carson et al. 2013), which correspond to the change in position angle (PA) of ΔPA $\sim 0\overset{\circ}{.}4$. Currie et al. (2018) observed the relative positions of κ And b in 2017 and derived the orbital parameters of κ And b from astrometric data prior to 2013 and their results (ΔPA $\sim 5\overset{\circ}{.}5$). We reanalyzed the orbital motion of κ And b using the relative positions of κ And b obtained by Subaru/HiCIAO+SCExAO in 2016 and Keck/NIRC2 in 2018. The PA change between the first Subaru/HiCIAO report and the latest NIRC2 data is $\sim 7°$.

ExoSOFT (Mede & Brandt 2017) was used for orbital fitting, which takes advantage of several techniques, including the Markov Chain Monte Carlo (MCMC) approach, to estimate dynamical parameters from relative positions at different epochs. First, we used two modules that are incorporated in ExoSOFT: simulated annealing to search for the global minimum and sigma tuning (ST) to determine reasonable step

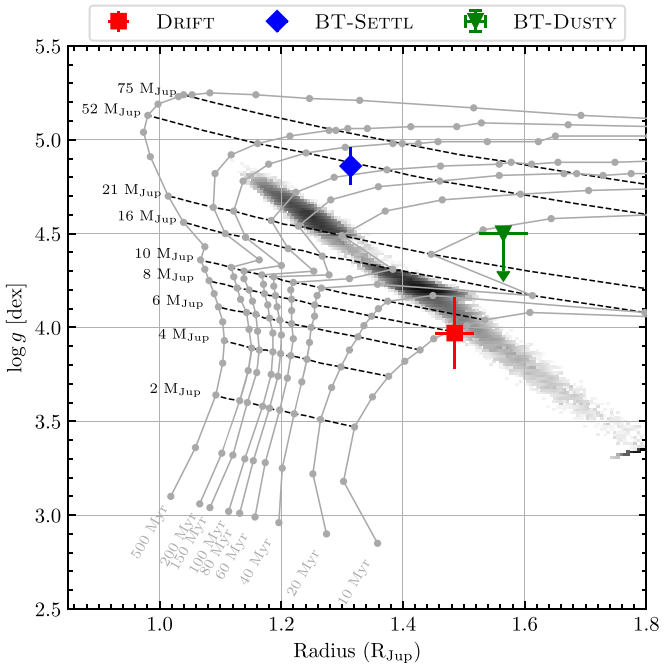

Figure 11. Radius–gravity diagram comparing the best-fit atmospheric models to isochrones (gray solid lines) and mass tracks (black dashed lines) from the COND03 evolutionary model (Baraffe et al. 2003). The radius and gravity derived via a Monte Carlo error propagation from the luminosity and age given in Currie et al. (2018) are also shown for comparison (gray-scale two-dimensional histogram), plotted on a logarithmic color scale to highlight the isoluminosity contour consistent with the measured luminosity of κ And b (Currie et al. 2018).

sizes. Finally, we ran *emcee* mode (an MCMC ensemble sampler; Foreman-Mackey et al. 2013) with $n = 6 \times 10^8$ total samples across 500 walkers to fit the orbit of κ And b and estimate its dynamical and orbital parameters. We adopted 19.3–20.7 mas for a parallax range and 2.65–2.95 $M_\odot$ for a mass range of the κ And system during the final fitting, as ExoSOFT does not currently allow those parameters to remain fixed when running in the *emcee* mode. The samples for the parameters (e, P, T_0, i, Ω, ω) were drawn from uniform proposal distributions. The priors for e, T_0, Ω, and ω were set as uniform, while we assumed a Jeffrey's prior function for the semimajor axis ($a^{-1}/\ln a_{\rm max}/a_{\rm min}$), with i and P given the priors $p(i) \propto \cos(i)$ and $p(P) \propto 1/P$, respectively. Providing only direct imaging data, orbital fitting using ExoSOFT finds the total mass of the κ And system ($m_{\rm total}$), although it is capable of solving for the individual masses when coupled with radial velocity (RV) data (see Section 2 of Mede & Brandt 2017, for more details).

Figure 12 and Table 7 show a result of the orbital fitting with ExoSOFT. The posteriors of the parameters used in ExoSOFT are shown in Figure 13. The mass ratio between the companion and the central star is $q \sim 0.005$, namely $m_{\rm total} \sim m_{\rm star}$. If the posterior function of $m_{\rm total}$ follows a Gaussian, we can estimate the dynamical mass of κ And A, which is independent of previous photometric/spectroscopic studies. However, our calculation could not robustly constrain $m_{\rm total}$ due to the limited number of κ And b locations. Our results of other orbital parameters achieved a best fit with a reduced χ^2 of 0.958 and are in good agreement with the previous report in Currie et al. (2018). In the ExoSOFT fit, the least convergent parameter was that of P having an integrated autocorrelation time of 921, equating to 6.5×10^5 effective samples. Astrometric monitoring for the next 10 yr is required to more accurately determine the orbital parameters of the κ And system.

6. Discussion

6.1. Formation and Evolution Scenario

Our atmospheric modeling favors 1700–1900 K, a surface gravity of $\log(g) \sim 4.0$–4.5, and a radius of 1.3–1.6 $R_{\rm Jup}$ with a cloudy atmosphere. The best-fit model (the DRIFT-PHOENIX model) is consistent with $\leqslant$40 Myr and $<$20 $M_{\rm Jup}$ in the evolutionary model. The object κ And b is a good laboratory for understanding the formation and an early stage of evolution of gas giant/low-mass brown dwarfs.

We reconfirmed that κ And b is likely to have a larger eccentricity and semimajor axis than GJ 504 b (Bonnefoy et al. 2018) and HR 8799 b, c, d, e (Wang et al. 2018). It may have experienced a strong excitation of the eccentricity by gravitational interactions between neighboring planets, such as planet–planet scattering. Planetesimal accretion and accumulation of disk gas cannot pump up the eccentricity of a planet's orbit up to $\sim$0.8. In fact, a wide orbit of κ And b cannot be reconciled with an in situ core accretion scenario. Although the minimum core mass for gas giant formation requires only a few Earth masses at $\sim$100 au (Piso & Youdin 2014), the core growth at 100 au takes a much longer time than the estimated age of the κ And system. Bonnefoy et al. (2014b) proposed another possible formation scenario for κ And b (i.e., a hot-start model); it may have formed via gravitational instability at almost the same orbital separation as the current location.

It may also be possible that κ And b was scattered to its current location (e.g., Marzari & Weidenschilling 2002; Ford & Rasio 2008; Nagasawa et al. 2008). Since the age of κ And A was estimated to be $\sim$40–50 Myr, dynamical instability was likely to have occurred if three or more giant planets coexisted in an outer region. An outwardly scattered planet, namely κ And b, can remain on a highly eccentric orbit because of less efficient/no dynamical friction damping of the eccentricity (Muto et al. 2011). To investigate this scenario, we consider that a planet–planet scattering event occurred after disk dispersal. The planet–planet scattering requires close encounters of planets, which are easily induced in a system of three or more planets. The behaviors of planet–planet scatterings that are involved in more than three planets need to be numerically examined by N-body simulations. In this study, we discuss a simple case with three giant planets. We assume (i) three massive gas giants/brown dwarfs are on nearly coplanar, circular, and tightly packed orbits around κ And; (ii) one of them is ejected from the system; (iii) κ And b is the outer planet of two remaining objects; (iv) the ejected planet has a smaller mass than κ And b (as shown by N-body simulations of planet–planet scatterings; Marzari & Weidenschilling 2002); and (v) the three objects have similar radii. Under these assumptions, we infer the mass and orbital elements of an unseen (potential) planet in the κ And system.

After dynamical instability happened, the eccentricity of an outer remaining object (κ And b) was determined by

$$e_{\rm out} \simeq \frac{m_{\rm in}}{m_{\rm out}} \times \sqrt{\frac{m_{\rm out} + m_{\rm eje}}{m_{\rm out} + m_{\rm in}}}, \quad (1)$$

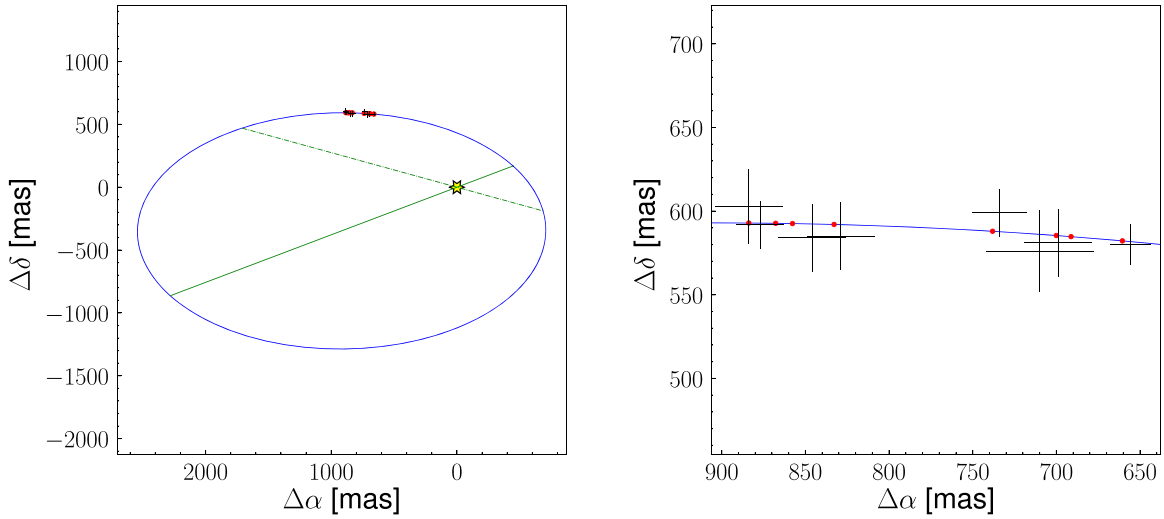

Figure 12. Orbital fitting of κ And b with ExoSOFT. A blue ellipse is the best-fit solution for the orbit of κ And b, where κ And b moves clockwise: (left) full orbit and (right) zoomed-in view near the current positions. Black plus signs are the relative positions of κ And b obtained by previous Subaru/Keck observations, and red points are the predicted locations of the best-fit orbit at each epoch. The solid and dashed lines in the left panel correspond to the projected semimajor axis and the line of nodes, respectively.

where m corresponds to the mass of an object and the subscripts "in," "out," and "eje" correspond to the inner, outer (κ And b), and ejected objects, respectively (Ida et al. 2013). Using Equation (1) and the mass and eccentricity of κ And b, i.e., $m_{\rm out} = 13\ M_{\rm Jup}$ and $e_{\rm out} = 0.77 \pm 0.08$, we can estimate the mass of the inner object as a function of the mass of the ejected object (see Table 8). We note that the error bar shown in Table 8 comes from only the error of eccentricity ExoSOFT provided. Estimating κ And b's mass largely depends on the age and evolutionary models, and we do not include this error. With these assumptions, the potential inner companion (planet) has a mass of $m_{\rm in} \gtrsim 10\ M_{\rm Jup}$. We note that Equation (1) is not applicable to the case where κ And initially had four or more giant planets in an outer region because the orbital evolution of such a system cannot be described analytically any longer.

Since no point source other than κ And b is seen in Figure 1, we discuss the mass limit of a detectable planet around κ And. The latest SCExAO+CHARIS observation reached a better contrast limit in the wavelength-collapsed image (Currie et al. 2018): ∼15, ∼8–10, and ∼3–5 $M_{\rm Jup}$ at 12.5, 25, and 50 au, respectively, using a hot-start model (COND03; Baraffe et al. 2003). With the deepest contrast limits around κ And, SCExAO+CHARIS observations can suggest that an inner companion can be located at $\lesssim$25 au.

Combining RV methods with direct imaging enables us to give stringent constraints on the orbital parameters of a substellar-mass companion (e.g., Bonnefoy et al. 2018; Calissendorff & Janson 2018). The lack of absorption lines obscures precise RV measurements of massive stars such as κ And A (∼B9 star) due to high temperature and rapid rotation. In fact, archival RV observations reported large errors, >1 km s^{-1} (Hinkley et al. 2013; Becker et al. 2015). Host-star astrometry is also useful, but estimating an accurate acceleration of such a bright star by a combination of *Gaia* and *Hipparcos* telescopes cannot avoid systematic errors between these telescopes (Brandt 2018). Accumulating *Gaia* data sets will possibly help to measure the dynamical mass of κ And b in the future.

6.2. Future Work

Spectral features of substellar-mass objects within ∼1–5 μm depend on molecular absorption, such as FeH, H_2O, KI, CH_4, and CO. Effective temperature, surface gravity, or C/O ratio parameters affect the IR spectrum (e.g., Sorahana & Yamamura 2012, 2014). Our study uses only photometry and low-resolution spectroscopy, which can induce degeneracy between $T_{\rm eff}$ and $\log g$ and the best-fit objects for the field-gravity objects in Figure 7. Although a precise determination of the gravity of κ And b will require higher spectral resolution observations, our measurements demonstrate that the object likely has a low surface gravity when considering the age of the system, consistent with the planetary mass predicted from a comparison with evolutionary models (e.g., Currie et al. 2018). For future work, as introduced in Currie et al. (2018), higher-resolution spectroscopy helps to investigate κ And b's atmosphere in detail. Subaru/CHARIS has another spectroscopic mode with high resolution ($R \sim 65$–75) in the J, H, and K bands.[25] Keck/OSIRIS could extract HR 8799 b's spectrum with higher resolution ($R = 4000$; Barman et al. 2015; Petit dit de la Roche et al. 2018). A mid-spectral-resolution integral field unit combined with AO has the capability to extract the detailed spectrum and investigate the atmospheric/evolutionary mechanisms of κ And b, as mentioned in Section 3.1. Furthermore, mid-IR (MIR) wavelength photometry/spectroscopy will also provide useful information. The *James Webb Space Telescope* (*JWST*)/MIRI is expected to obtain untouched atmospheric parameters of exoplanets at MIR, such as NH_3, CH_4, H_2O, CO_2, and PH_3 (Danielski et al. 2018). Combining these follow-up observations will provide improved models for κ And b.

We also investigate the possibility of detecting a potential inner planet. The RV and host-star astrometry are more sensitive to close-in planets than direct imaging. However, as mentioned in Section 6.1, it is difficult for these methods to search for inner planets around κ And. As we could not constrain an inclination of the potential inner planet, transit observation is almost a blind search. Future high-contrast

[25] https://scholar.princeton.edu/charis/capabilities

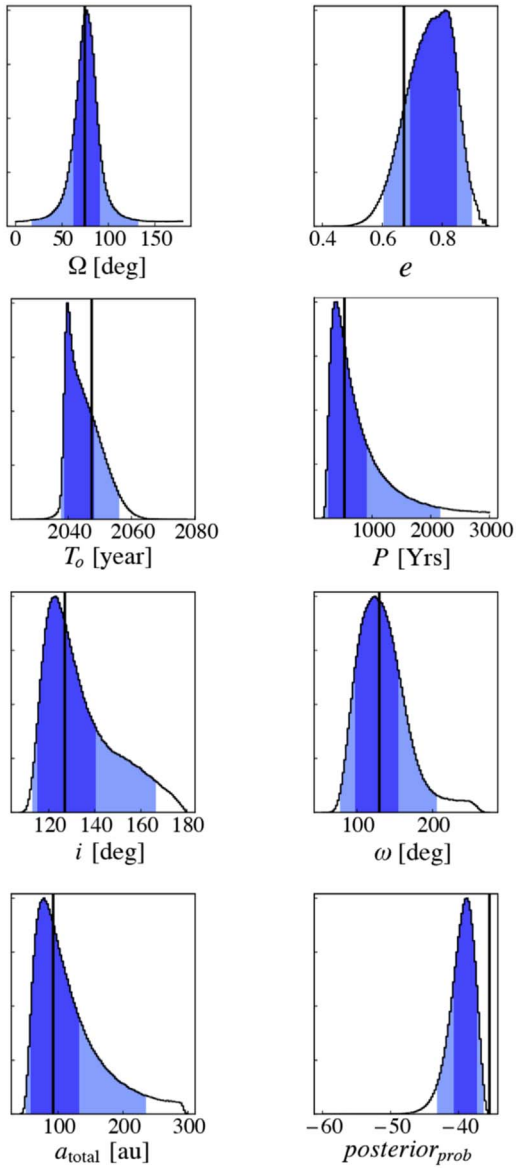

Figure 13. Posteriors of MCMC parameters used in ExoSOFT for the κ And system. Dark and light blue regions correspond to 1σ and 2σ, respectively. Solid black lines represent best-fit values of each parameter (where "best-fit" refers to the orbital parameter set with the lowest χ^2 value).

Table 7
Orbital Parameters of κ And b

Parameter	Median	68% Confidence Level	95% Confidence Level
a_{tot} [au]	103.6	[57.4, 133.4]	[50.3, 236.0]
P [yr]	631.1	[242.4, 900.4]	[198.6, 2148.9]
e	0.77	[0.69, 0.85]	[0.60, 0.90]
i [deg]	130.0	[114.9, 140.0]	[112.6, 166.6]
ω [deg]	130.7	[96.6, 155.4]	[77.0, 205.0]
Ω [deg]	76.5	[61.3, 90.5]	[16.4, 132.1]
T_0 [yr]	2044.1	[2038.4, 2047.9]	[2037.5, 2056.3]

imaging instruments with a better contrast level and inner working angle, e.g., the Thirty Meter Telescope (TMT), will help to search for inner planets and promote orbital evolution mechanisms of κ And b. Continuing direct imaging with current ground-based telescopes also helps to add further plots of κ And b for better orbital fitting.

Table 8
Mass Estimation of a Potential Inner Companion around κ And

Ejected Object [M_{Jup}]	Inner Object [M_{Jup}]
2	$13.2^{+1.9}_{-1.7}$
4	$12.2^{+1.7}_{-1.6}$
6	$11.3^{+1.6}_{-1.5}$
8	10.6 ± 1.4
10	$10.0^{+1.4}_{-1.3}$

7. Conclusion

We used Subaru/SCExAO+HiCIAO and Keck/NIRC2 to investigate κ And b's SED and fit the orbit by gathering our results and previous high-contrast imaging studies. We detected κ And b with S/Ns of ~130 and 10 in the HiCIAO H and Y bands and ~13 in the NIRC2 K_s band. The Y-band photometry was combined with previous photometric/spectroscopic studies for an empirical comparison with spectral templates and synthetic SED modeling with atmospheric models. Empirical comparisons showed that κ And b is likely a low-gravity object, albeit one with a slightly wider range of plausible spectral types than previously inferred (L0–L2 instead of L0–L1). We also investigated the gravitational scores of the library objects and found that the best-fit objects may give lower gravity than previously reported.[26] The best fit among the models used is the DRIFT-PHOENIX model at $T_{eff} = 1700$ K and $\log g = 4.0$ [dex]. With the interpolated grid, the best fit is located at $T_{eff} = 1739$ K and $\log g = 4.0$ [dex]. More than 7 yr have passed since the first report of κ And b in 2011 January, which resulted in a PA change of PA $\sim 7°$. By running ExoSOFT, we found that the orbit is likely highly eccentric, which suggests a possibility that κ And b has experienced orbital migration due to planet–planet scattering. Our detection limit could partially set a constraint on the existence of a potential inner companion. The orbital fitting section in this paper follows their discussions. Our analysis will help to update the synthetic understanding of the formation and evolution mechanism of the κ And system.

For future work, spectroscopic studies with higher resolution, such as the high-resolution mode of Subaru/CHARIS or Keck/OSIRIS, will help to investigate κ And b's atmosphere in detail. The *JWST* will enable one to obtain spectral/photometric information at MIR. The TMT is expected to achieve a higher enough contrast to detect inner planetary-mass objects and update the orbital discussions. Our work motivates follow-up observations for future telescopes and further discussion of the formation/evolution mechanisms of κ And b.

The authors would like to thank the anonymous referees for their constructive comments and suggestions to improve the quality of the paper. This paper is based in part on data collected at the Subaru Telescope and obtained from SMOKA,

[26] Some intermediate-gravity dwarfs also provide good fits to the κ And b spectrum. However, we did not take into account information about the system's age in our fitting (i.e., we did not impose a "prior" on the gravity classification of "b" given the age of the primary). Doing so would have even more strongly favored low-gravity objects.

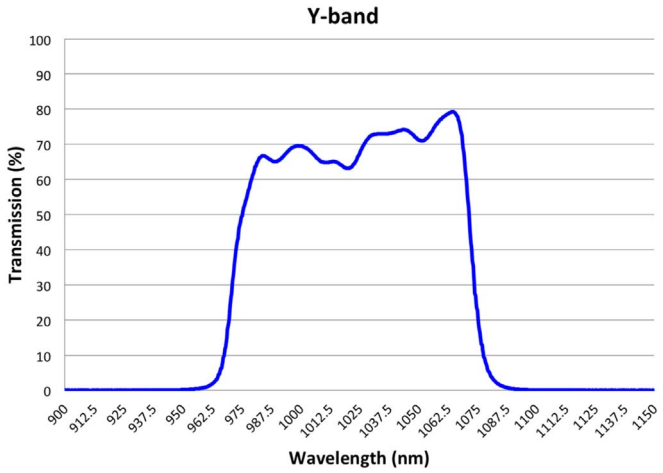

Figure 14. Transmission of the *Y*-band test filter under 77 K.

which is operated by the Astronomy Data Center, National Astronomical Observatory of Japan. Some of the data presented herein were obtained at the W. M. Keck Observatory, which is operated as a scientific partnership among the California Institute of Technology, the University of California, and the National Aeronautics and Space Administration. The observatory was made possible by the generous financial support of the W. M. Keck Foundation. This work presents results from the European Space Agency (ESA) space mission *Gaia*. The *Gaia* data are being processed by the *Gaia* Data Processing and Analysis Consortium (DPAC). Funding for the DPAC is provided by national institutions, in particular the institutions participating in the *Gaia* Multilateral Agreement (MLA). The *Gaia* mission website is https://www.cosmos.esa.int/gaia. The *Gaia* archive website is https://archives.esac.esa.int/gaia.

T.U. acknowledges a JSPS overseas research fellowship. This work was supported by JSPS KAKENHI grant Nos. JP17J00934, 15H02063, and 18H05442. T.C. was supported by a NASA Senior Postdoctoral Fellowship and NASA/Keck grant LK-2663-948181; R.D.R. was supported by NASA grant NSSC17K0535. The development of SCExAO was supported by JSPS (Grant-in-Aid for Research Nos. 23340051, 26220704, and 23103002), the Astrobiology Center of NINS, Japan, the Mt. Cuba Foundation, and the director's contingency fund at the Subaru Telescope. CHARIS was developed with the support of Grant-in-Aid for Scientific Research on Innovative Areas No. 2302.

The authors wish to acknowledge the very significant cultural role and reverence that the summit of Maunakea has always had within the indigenous Hawaiian community. We are most fortunate to have the opportunity to conduct observations from this mountain.

Appendix
HiCIAO Filter Transmission

In Figure 14, we show the transmission of a *Y*-band test filter that has almost the same specifications as HiCIAO. The HiCIAO observations were basically carried out with an optical bench temperature of ~80 K, and this filter transmission is measured under 77 K.

ORCID iDs

Taichi Uyama https://orcid.org/0000-0002-6879-3030
Thayne Currie https://orcid.org/0000-0002-7405-3119
Yasunori Hori https://orcid.org/0000-0003-4676-0251
Robert J. De Rosa https://orcid.org/0000-0002-4918-0247
Kyle Mede https://orcid.org/0000-0003-1329-0409
Timothy D. Brandt https://orcid.org/0000-0003-2630-8073
Jungmi Kwon https://orcid.org/0000-0003-2815-7774
Olivier Guyon https://orcid.org/0000-0002-1097-9908
Frantz Martinache https://orcid.org/0000-0003-1180-4138
Tomoyuki Kudo https://orcid.org/0000-0002-9294-1793
Motohide Tamura https://orcid.org/0000-0002-6510-0681
Jeffrey Chilcote https://orcid.org/0000-0001-6305-7272
Ruben Asensio-Torres https://orcid.org/0000-0003-2990-0726
Markus Janson https://orcid.org/0000-0001-8345-593X
Gillian R. Knapp https://orcid.org/0000-0002-9259-1164

References

Allard, F., Hauschildt, P. H., Alexander, D. R., Tamanai, A., & Schweitzer, A. 2001, ApJ, 556, 357
Allard, F., Homeier, D., & Freytag, B. 2012, RSPTA, 370, 2765
Allers, K. N., & Liu, M. C. 2013, ApJ, 772, 79
Asplund, M., Grevesse, N., Sauval, A. J., & Scott, P. 2009, ARA&A, 47, 481
Baraffe, I., Chabrier, G., Barman, T. S., Allard, F., & Hauschildt, P. H. 2003, A&A, 402, 701
Barber, R. J., Tennyson, J., Harris, G. J., & Tolchenov, R. N. 2006, MNRAS, 368, 1087
Bardalez Gagliuffi, D. C., Burgasser, A. J., Gelino, C. R., et al. 2014, ApJ, 794, 143
Barman, T. S., Konopacky, Q. M., Macintosh, B., & Marois, C. 2015, ApJ, 804, 61
Becker, J. C., Johnson, J. A., Vanderburg, A., & Morton, T. D. 2015, ApJS, 217, 29
Bell, C. P. M., Mamajek, E. E., & Naylor, T. 2015, MNRAS, 454, 593
Blunt, S., Nielsen, E. L., De Rosa, R. J., et al. 2017, AJ, 153, 229
Boley, A. C. 2009, ApJL, 695, L53
Bonnefoy, M., Chauvin, G., Lagrange, A.-M., et al. 2014a, A&A, 562, 127
Bonnefoy, M., Currie, T., Marleau, G. D., et al. 2014b, A&A, 562, A111
Bonnefoy, M., Perraut, K., Lagrange, A. M., et al. 2018, A&A, 618, A63
Bonnefoy, M., Zurlo, A., Baudino, J. L., et al. 2016, A&A, 587, A58
Boss, A. P. 2011, ApJ, 731, 74
Bowler, B. P. 2016, PASP, 128, 102001
Brandt, T. D. 2018, ApJS, 239, 31
Brandt, T. D., McElwain, M. W., Turner, E. L., et al. 2014, ApJ, 794, 159
Burgasser, A. J. 2007, ApJ, 659, 655
Burgasser, A. J. 2014, in ASI Conf. Ser. 11, International Workshop on Stellar Spectral Libraries, ed. H. P. Singh, P. Prugniel, & I. Vauglin (Pune: ASI), 7
Burgasser, A. J., Cruz, K. L., Cushing, M., et al. 2010, ApJ, 710, 1142
Burgasser, A. J., Liu, M. C., Ireland, M. J., Cruz, K. L., & Dupuy, T. J. 2008, ApJ, 681, 579
Burgasser, A. J., & McElwain, M. W. 2006, AJ, 131, 1007
Burrows, A., Sudarsky, D., & Hubeny, I. 2006, ApJ, 640, 1063
Caffau, E., Ludwig, H. G., Steffen, M., Freytag, B., & Bonifacio, P. 2011, SoPh, 268, 255
Calissendorff, P., & Janson, M. 2018, A&A, 615, A149
Carson, J., Thalmann, C., Janson, M., et al. 2013, ApJL, 763, L32
Chauvin, G., Desidera, S., Lagrange, A. M., et al. 2017, A&A, 605, L9
Cheetham, A., Bonnefoy, M., Desidera, S., et al. 2018, A&A, 615, A160
Chilcote, J., Pueyo, L., De Rosa, R. J., et al. 2017, AJ, 153, 182
Chiu, K., Fan, X., Leggett, S. K., et al. 2006, AJ, 131, 2722
Cruz, K. L., Kirkpatrick, J. D., & Burgasser, A. J. 2009, AJ, 137, 3345
Cruz, K. L., Núñez, A., Burgasser, A. J., et al. 2018, AJ, 155, 34
Currie, T., Brandt, T. D., Uyama, T., et al. 2018, AJ, 156, 291
Currie, T., Burrows, A., & Daemgen, S. 2014a, ApJ, 787, 104
Currie, T., Burrows, A., Itoh, Y., et al. 2011, ApJ, 729, 128
Currie, T., Burrows, A., Madhusudhan, N., et al. 2013, ApJ, 776, 15
Currie, T., Cloutier, R., Brittain, S., et al. 2015, ApJL, 814, L27
Currie, T., Daemgen, S., Debes, J., et al. 2014b, ApJL, 780, L30
Currie, T., Debes, J., Rodigas, T. J., et al. 2012a, ApJL, 760, L32

Currie, T., Fukagawa, M., Thalmann, C., Matsumura, S., & Plavchan, P. 2012b, ApJL, 755, L34
Currie, T., Guyon, O., Lozi, J., et al. 2019a, arXiv:1909.10522
Currie, T., Guyon, O., Tamura, M., et al. 2017, ApJL, 836, L15
Currie, T., Hernandez, J., Irwin, J., et al. 2010, ApJS, 186, 191
Currie, T., Marois, C., Cieza, L., et al. 2019b, ApJL, 877, L3
Cushing, M. C., Rayner, J. T., & Vacca, W. D. 2005, ApJ, 623, 1115
Cutri, R. M., Skrutskie, M. F., van Dyk, S., et al. 2003, yCat, 2246, 0
Danielski, C., Baudino, J.-L., Lagage, P.-O., et al. 2018, AJ, 156, 276
De Rosa, R. J., Rameau, J., Patience, J., et al. 2016, ApJ, 824, 121
Filippazzo, J. C., Rice, E. L., Faherty, J., et al. 2015, ApJ, 810, 158
Ford, E. B., & Rasio, F. A. 2008, ApJ, 686, 621
Foreman-Mackey, D., Hogg, D. W., Lang, D., & Goodman, J. 2013, PASP, 125, 306
Fortney, J. J., Marley, M. S., Saumon, D., & Lodders, K. 2008, ApJ, 683, 1104
Gagné, J., Faherty, J. K., Cruz, K. L., et al. 2015, ApJS, 219, 33
Gagné, J., Mamajek, E. E., Malo, L., et al. 2018, ApJ, 856, 23
Gaia Collaboration, Brown, A. G. A., Vallenari, A., et al. 2018, A&A, 616, A1
Garcia, E. V., Currie, T., Guyon, O., et al. 2017, ApJ, 834, 162
Hauschildt, P. H. 1992, JQSRT, 47, 433
Hinkley, S., Pueyo, L., Faherty, J. K., et al. 2013, ApJ, 779, 153
Hubeny, I., & Lanz, T. 1995, ApJ, 439, 875
Ida, S., Lin, D. N. C., & Nagasawa, M. 2013, ApJ, 775, 42
Janson, M., Asensio-Torres, R., André, D., et al. 2019, A&A, 626, A99
Jones, J., White, R. J., Quinn, S., et al. 2016, ApJL, 822, L3
Kellogg, K., Metchev, S., Miles-Páez, P. A., & Tannock, M. E. 2017, AJ, 154, 112
Keppler, M., Benisty, M., Müller, A., et al. 2018, A&A, 617, A44
Kirkpatrick, J. D. 2005, ARA&A, 43, 195
Kirkpatrick, J. D., Barman, T. S., Burgasser, A. J., et al. 2006, ApJ, 639, 1120
Kirkpatrick, J. D., Looper, D. L., Burgasser, A. J., et al. 2010, ApJS, 190, 100
Kühn, J., Serabyn, E., Lozi, J., et al. 2018, PASP, 130, 035001
Kuzuhara, M., Tamura, M., Kudo, T., et al. 2013, ApJ, 774, 11
Lachapelle, F.-R., Lafrenière, D., Gagné, J., et al. 2015, ApJ, 802, 61
Lafrenière, D., Marois, C., Doyon, R., Nadeau, D., & Artigau, É. 2007, ApJ, 660, 770
Lagrange, A.-M., Bonnefoy, M., Chauvin, G., et al. 2010, Sci, 329, 57
Liu, M. C., Dupuy, T. J., & Allers, K. N. 2016, ApJ, 833, 96
Liu, M. C., Magnier, E. A., Deacon, N. R., et al. 2013, ApJL, 777, L20
Macintosh, B., Graham, J. R., Barman, T., et al. 2015, Sci, 350, 64
Marois, C., Lafrenière, D., Doyon, R., Macintosh, B., & Nadeau, D. 2006, ApJ, 641, 556
Marois, C., Zuckerman, B., Konopacky, Q. M., Macintosh, B., & Barman, T. 2010, Natur, 468, 1080
Marzari, F., & Weidenschilling, S. J. 2002, Icar, 156, 570
Mede, K., & Brandt, T. D. 2017, AJ, 153, 135
Muto, T., Takeuchi, T., & Ida, S. 2011, ApJ, 737, 37
Nagasawa, M., Ida, S., & Bessho, T. 2008, ApJ, 678, 498
Nielsen, E. L., De Rosa, R. J., Macintosh, B., et al. 2019, AJ, 158, 13
Partridge, H., & Schwenke, D. W. 1997, JChPh, 106, 4618
Patience, J., King, R. R., De Rosa, R. J., et al. 2012, A&A, 540, A85
Pecaut, M. J., & Mamajek, E. E. 2013, ApJS, 208, 9
Petit dit de la Roche, D. J. M., Hoeijmakers, H. J., & Snellen, I. A. G. 2018, A&A, 616, A146
Pickles, A., & Depagne, É 2010, PASP, 122, 1437
Piso, A.-M. A., & Youdin, A. N. 2014, ApJ, 786, 21
Pollack, J. B., Hubickyj, O., Bodenheimer, P., et al. 1996, Icar, 124, 62
Rajan, A., Rameau, J., De Rosa, R. J., et al. 2017, AJ, 154, 10
Reid, I. N., Lewitus, E., Burgasser, A. J., & Cruz, K. L. 2006, ApJ, 639, 1114
Robert, J., Gagné, J., Artigau, É., et al. 2016, ApJ, 830, 144
Sorahana, S., & Yamamura, I. 2012, ApJ, 760, 151
Sorahana, S., & Yamamura, I. 2014, ApJ, 793, 47
Tamura, M. 2009, in AIP Conf. Ser. 1158, Exoplanets and Disks: Their Formation and Diversity: Proceedings of the International Conference, ed. M. Usuda, M. Tamura, & M. Ishii (Melville, NY: AIP), 11
Tokunaga, A. T., Simons, D. A., & Vacca, W. D. 2002, PASP, 114, 180
Uyama, T., Hashimoto, J., Kuzuhara, M., et al. 2017, AJ, 153, 106
Wang, J. J., Graham, J. R., Dawson, R., et al. 2018, AJ, 156, 192
Witte, S., Helling, C., Barman, T., Heidrich, N., & Hauschildt, P. H. 2011, A&A, 529, A44